



Article

Assessing the Impact of Extreme Droughts on Dryland Vegetation by Multi-Satellite Solar-Induced Chlorophyll Fluorescence

Song Leng ^{1,2} , Alfredo Huete ² , Jamie Cleverly ³, Sicong Gao ⁴ , Qiang Yu ^{2,5}, Xianyong Meng ⁶, Junyu Qi ⁷, Rongrong Zhang ¹ and Qianfeng Wang ^{1,8,*}

- ¹ Fujian Provincial Key Laboratory of Remote Sensing of Soil Erosion, College of Environment & Safety Engineering, Fuzhou University, Fuzhou 350116, China; song.leng@student.uts.edu.au (S.L.); n190620018@fzu.edu.cn (R.Z.)
- ² School of Life Sciences, University of Technology Sydney, Ultimo, NSW 2007, Australia; alfredo.huete@uts.edu.au (A.H.); qiang.yu@uts.edu.au (Q.Y.)
- ³ College of Science and Engineering, James Cook University, Cairns, QLD 4878, Australia; dr.jr.cleverly@gmail.com
- ⁴ Land and Water, Commonwealth Scientific and Industrial Research Organization, Adelaide, SA 5064, Australia; steve.gao@csiro.au
- ⁵ State Key Laboratory of Soil Erosion and Dryland Farming on the Loess Plateau, Northwest A&F University, Xianyang 712100, China
- ⁶ School of Atmospheric Physics, Nanjing University of Information Science & Technology, Nanjing 210044, China; xymeng@nuist.edu.cn
- ⁷ Earth System Science Interdisciplinary Center, University of Maryland, College Park, MD 20740, USA; junyuqi@umd.edu
- ⁸ Key Lab of Spatial Data Mining & Information Sharing, Ministry of Education of China, Fuzhou 350116, China
- * Correspondence: wangqianfeng@fzu.edu.cn



Citation: Leng, S.; Huete, A.; Cleverly, J.; Gao, S.; Yu, Q.; Meng, X.; Qi, J.; Zhang, R.; Wang, Q. Assessing the Impact of Extreme Droughts on Dryland Vegetation by Multi-Satellite Solar-Induced Chlorophyll Fluorescence. *Remote Sens.* **2022**, *14*, 1581. <https://doi.org/10.3390/rs14071581>

Academic Editors: Jingzhe Wang, Zhongwen Hu, Yangyi Wu and Jie Zhang

Received: 5 March 2022

Accepted: 22 March 2022

Published: 25 March 2022

Publisher's Note: MDPI stays neutral with regard to jurisdictional claims in published maps and institutional affiliations.



Copyright: © 2022 by the authors. Licensee MDPI, Basel, Switzerland. This article is an open access article distributed under the terms and conditions of the Creative Commons Attribution (CC BY) license (<https://creativecommons.org/licenses/by/4.0/>).

Abstract: Satellite-estimated solar-induced chlorophyll fluorescence (SIF) is proven to be an effective indicator for dynamic drought monitoring, while the capability of SIF to assess the variability of dryland vegetation under water and heat stress remains challenging. This study presents an analysis of the responses of dryland vegetation to the worst extreme drought over the past two decades in Australia, using multi-source spaceborne SIF derived from the Global Ozone Monitoring Experiment-2 (GOME-2) and Tropospheric Monitoring Instrument (TROPOMI). Vegetation functioning was substantially constrained by this extreme event, especially in the interior of Australia, in which there was hardly seasonal growth detected by neither satellite-based observations nor tower-based flux measurements. At a 16-day interval, both SIF and enhanced vegetation index (EVI) can timely capture the reduction at the onset of drought over dryland ecosystems. The results demonstrate that satellite-observed SIF has the potential for characterizing and monitoring the spatiotemporal dynamics of drought over water-limited ecosystems, despite coarse spatial resolution coupled with high-retrieval noise as compared with EVI. Furthermore, our study highlights that SIF retrieved from TROPOMI featuring substantially enhanced spatiotemporal resolution has the promising capability for accurately tracking the drought-induced variation of heterogeneous dryland vegetation.

Keywords: dryland; SIF; EVI; TROPOMI; extreme drought

1. Introduction

Large-scale drought, as one of most costly and pressing natural hazards, has profound impacts on terrestrial ecosystems, water resource, agriculture, and social economics [1]. In addition, global warming increases the exposure frequency to extreme heatwaves, which raises the risk of water deficit and leads to substantial losses of vegetation production [2,3]. As a consequence of highly variable climate, Australia is particularly vulnerable to extreme drought, as evidenced by Millennium Drought (2001–2009) in the Murray–Darling basin

as well as the 2012–2013 drought over arid inland [4,5]. Australia tends to be a global hot spot for variability, with semiarid vegetation in that country exhibiting increased carbon uptake [6]. By persisting through the ‘big dry’ and responding favorably in a following ‘big wet’ [7], Australia’s ecosystems play a significant role in regulating the global water and carbon cycles [4]. Enhancing our understanding with respect to dryland ecosystem in response to climate extreme is paramount for effectively managing the environment and global change research [8–11].

Satellite-based observation offers a method for monitoring and characterizing the spatiotemporal dynamics of vegetation under changing climates [12], which is especially valuable for remote areas such as most Australia’s interior with very sparse monitoring sites. Traditional reflectance-based vegetation indices are widely applied to assess the effects of extreme drought on ecosystem functioning and vegetation productivity at a regional, continental, or global scale [8,13–17]. Dramatic impacts of climate extremes on vegetation dynamics (as measured by EVI) with abrupt changes in phenology and productivity over southeast Australia demonstrates that semiarid ecosystems exhibit the largest sensitivity to hydro-climatic variations [18,19]. Although vegetation-index-based approaches are essential for evaluating vegetation variation under large-scale drought events, the observations they provide are not directly associated with vegetation functioning [20].

During recent years, satellite retrievals of SIF based on energy reemitted directly from the core of photosynthetic machinery present a fresh manner to observe vegetation growth and response [21–23]. On account of energy conservation, variations in SIF signal include information regarding vegetation physiological, biochemical, and metabolic functions in addition to the amount of absorbed photosynthetically active radiation [20]. Numerous studies have examined the relationship between GPP and SIF for each biome at various scales retrieved from different satellite sensors [24–27], implying that SIF can be unbiased in monitoring of vegetation productivity and further contribute to the understanding of the global terrestrial carbon cycle [28,29]. Both SIF and Moderate Resolution Imaging Spectroradiometer (MODIS) GPP respond to water availability in much the same direction beyond their previously determined correlations, although biome-specific distinction remains evident [30].

Relative to traditional vegetation indices (e.g., normalized difference vegetation index, enhanced vegetation index, leaf area index, etc.), spaceborne SIF or fluorescence yield was found to show an earlier and more significant response to rainfall deficits and heat stress over tropical vegetated region, forest, and cropland at monthly scale [31,32]. It highlights that SIF is susceptible to both the structural and physiological variations of vegetation and can be beneficial to timely monitor and characterize the development of drought and heatwave [33–35]. During the extreme drought of 2015–2016 driven by a strong El Nino event, large-scale decoupling of greenness and photosynthesis over Amazon forests was observed by satellite, of which SIF showed a pronounced reduction as opposed to a slight increase of canopy greenness [36]. The magnitude of divergence in greenness and photosynthesis that are related to times of fluctuant soil moisture differ in sign along a tree cover gradient, and those of forested ecosystems display contrasting average responses [37]. Conversely, both greenness and photosynthesis of non-woody semiarid ecosystems exhibiting a strong response to the availability of soil moisture usually alter contemporaneously [37]. To assess the effect of drought-related stress, there is a need for remotely sensed indicators that measure not only how green the plants are, but also to what extent photosynthetic activity is.

By investigating the response of vegetation growth to the 2019 extreme heatwave in Australia, Qiu et al. [38] concluded that SIF observed by both GOME-2 and Orbiting Carbon Observatory-2 (OCO-2) are more sensitive to water and heat stress than the greenness-based vegetation index (EVI). In addition, OCO-2 SIF exhibits a more pronounced decrease and one-month earlier than GOME-2 SIF, primarily owing to the diverse timing of observations (overpass timing: GOME-2 at near 09:30 a.m. and OCO-2 at 1:36 p.m. local solar time). Nonetheless, this study was conducted with limited baseline years (2015–2019), and it

remains uncertain at a relatively coarse scale (1° spatial resolution and monthly interval) for heterogeneous Australia's dryland vegetation under highly dynamic climate. The newly launched TROPOMI facilitates a considerable enhancement in SIF observation as a result of unprecedented spatial resolution (up to $7\text{ km} \times 3.5\text{ km}$ at nadir) and near-daily global coverage as contrasted with GOME-2 and OCO-2 [26,39], which enables the assessment of the relationship of SIF-GPP at an ecologically meaningful scale.

Characteristic drought time-scale can play a critical role in determining the sensitivity of biome-specific vegetation to drought [40]. Arid and humid biomes mostly respond to short time-scales, while semiarid and subhumid biomes respond to long time scales [40]. The response of the annual crop yield in five main dryland cultivations in the United States to different time-scales of drought is highly spatial variable, of which some crops (e.g., winter wheat) responded to drought at medium to long SPEI time-scales, while other crops (e.g., soybean and corn) responded to short or long drought time-scales [41]. It remains unclear how major biome types of natural dryland vegetation respond to drought at different intensities and time scales.

Here, we utilize the large-scale 2018–2019 drought across Australia as a natural experiment to investigate and characterize the spatiotemporal response of dryland vegetation to this extreme event, using multiple-source satellite observations of solar-induced chlorophyll fluorescence and vegetation greenness. Specifically, our objectives are: (1) to investigate the spatiotemporal variability of photosynthesis and greenness of Australia's dryland vegetation under 2018–2019 extreme drought; (2) to examine whether SIF could earlier capture drought stress than EVI at monthly/semi-monthly scale; (3) to assess the capability of SIF retrieved from TROPOMI for dynamic drought monitoring over water-limited ecosystems.

2. Materials and Methods

2.1. Study Area

This study was conducted at a sub-continental scale between 10°S to 26°S and 113°E to 138°E , which encompassed northern and central Australia by a relatively constant decrease in rainfall with distance inland (Figure 1). This region, particularly for northern Australia, has a classic monsoon climate pattern, which receives more than 80% of annual precipitation during November to April [42]. From northern mesic tropics to the xeric central Australia, mean annual rainfall ranges from 1700 mm to approximately 300 mm (Bureau of Meteorology, Available online: <https://www.bom.gov.au> (accessed on 20 January 2020)), in line with the aridity index (AI) decreasing from 0.8 to 0.1 (Figure 1b). Correspondingly, the vegetation follows a wet–dry gradient that shifts from *Eucalyptus* dominated forests, open forests, and woodlands in the coastal northern areas to *Acacia*-dominated open woodlands, scattered shrubs, and hummock grassland into the vast inland [42] (Figure 1a).

To assess satellite observation with ground-based evidence, we selected five representative flux tower sites across the extensive study area: Howard Springs (AU-How), Dry River (AU-Dry), Sturt Plains (AU-Stp), Alice Spring Mulga (AU-ASM), and Ti Tree East (AU-TTE) [43]. The detailed description of five sites is shown in Table 1 (Available online: www.ozflux.org.au (accessed on 15 July 2019)). Apart from two northern sites (AU-How and AU-Dry), the remaining sites in the interior of Australia experienced extreme drought in 2018–2019.

Table 1. Summary of five eddy covariance flux tower sites.

Site	Abbreviation	Longitude ($^\circ\text{E}$)	Latitude ($^\circ\text{S}$)	Vegetation Type	Data Coverage
Howard Springs	AU-How	131.15	12.495	Eucalypt woodlands	2001–2019
Dry River	AU-Dry	132.371	15.259	Open forest savanna	2008–2019
Sturt Plains	AU-Stp	133.3502	17.1507	Tussock grasslands	2008–2018
Alice Spring Mulga	AU-ASM	133.2493	22.2828	<i>Acacia</i> woodlands	2010–2019
Ti Tree East	AU-TTE	133.64	22.287	<i>Corymbia</i> savanna	2012–2019

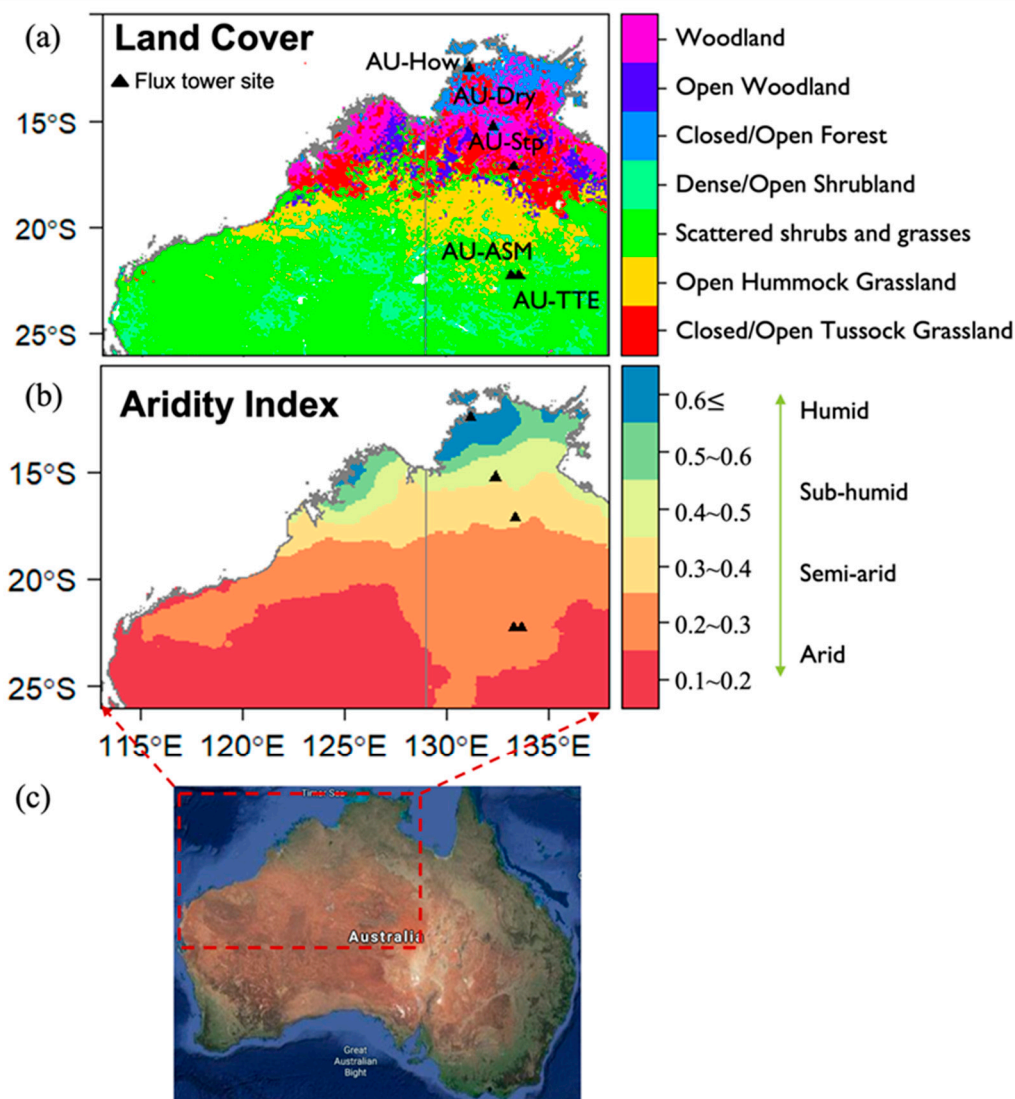


Figure 1. (a) Land cover map based on national Dynamic Land Cover Dataset. (b) Spatial pattern of aridity index. (c) The locations of study area over Australian continent (image source: Google Earth). Black triangles refer to five flux tower sites.

2.2. Satellite Data

A summary of satellite-based datasets used in this study is shown in Table 2. We utilized two sets of satellite-based SIF records. (1) The first dataset was obtained from Global Ozone Monitoring Experiment-2 onboard EUMETSAT's MetOp-A as well as MetOp-B platform (indicated as GOME-2A and GOME-2B, respectively, in this study). SIF is the retrieval of the far-red chlorophyll fluorescence peaking at 740 nm, based on a simplified radiative transfer model in the company of a principal component analysis [44]. Monthly global coverage of SIF data based on GOME-2A at 0.5° spatial resolution (Level 3, Version 28) from February 2007 to March 2019 was obtained from NASA Goddard Space Flight Centre (Available online: <https://avdc.gsfc.nasa.gov/> (accessed on 10 May 2020)). Given the degradation of the GOME-2A instrument during its lifetime, SIF observed from GOME-2B was also downloaded, which spans from March 2013 to March 2019. The daily orbital data (Level 2, Version 28) was also used to aggregate 16-day interval records for higher temporal-resolution analysis. (2) We used a newly released SIF dataset based on TROPOMI onboard the Sentinel-5 Precursor satellite. A data-driven method was employed to retrieve the SIF signal using spectral measurements ranging from 743 nm to 758 nm [26]. Daily corrected ungirded TROPOMI SIF data at a 0.05° spatial resolution (2018–2019) was

available at (Available online: <ftp://fluو.gps.caltech.edu/data/tropomi/> (accessed on 1 December 2020)). The daily orbital TROPOMI SIF were likewise aggregated to monthly and 16-day series by mean value, consistent with temporal resolution of GOME-2 SIF records.

Table 2. Summary of satellite-based datasets.

Dataset	Source	Resolution	Data Coverage
solar-induced chlorophyll fluorescence (SIF)	GOME-2 (MetOp-A)	Monthly/daily, 0.5°	2007–2019
solar-induced chlorophyll fluorescence (SIF)	GOME-2 (MetOp-B)	Monthly/daily, 0.5°	2013–2019
solar-induced chlorophyll fluorescence (SIF)	TROPOMI (Sentinel-5 Precursor)	Monthly/daily, 0.05°	2018–2019
enhanced vegetation index (EVI)	MODIS (Aqua)	Monthly/16-day, 0.05°	2007–2019
gross primary productivity (GPP)	FluxSat (MODIS and FLUXNET 2015)	Monthly, 0.5°	2007–2019
photosynthetic active radiation (PAR)	CERES (Aqua)	Monthly, 1°	2007–2019
land surface temperature (LST)	MODIS (Aqua)	Monthly, 0.05°	2007–2019
Precipitation	IMERG (GPM)	Monthly, 0.1°	2007–2019

We used Moderate Resolution Imaging Spectroradiometer (MODIS on board Aqua, Collection 6) MYD13C1 (0.05°, 16-day) and MYD13C2 (0.05°, monthly) Vegetation Indices products from January 2007 to June 2019 downloaded from NASA Earth Observation data (Available online: <https://search.earthdata.nasa.gov/search> (accessed on 1 August 2020)). EVI is an optimized version of vegetation indices that effectively reduces soil background influences and is widely used as a proxy of canopy greenness [45–47]. The equation (1) of EVI is:

$$EVI = 2.5 \frac{\rho_{NIR} - \rho_{red}}{\rho_{NIR} + 6\rho_{red} - 7.5\rho_{blue} + 1} \quad (1)$$

where ρ_{blue} , ρ_{red} , ρ_{NIR} are reflectance in the blue, red, and near infrared bands, respectively. To reduce noise and uncertainties, only best quality data remained in this study through removing pixels of which quality control flag of the first 2 bits neither 00 nor 01, and pixel-wise EVI time series data was smoothed using the Savitzky–Golay filter.

To contrast with satellite-observed greenness and fluorescence, data-driven gross primary productivity (FluxSat_GPP, version 1.1, 2007–2019) derived primarily from MODIS reflectance product was used as the spatial reference of vegetation activity, obtained from NASA Goddard Space Flight Centre (Available online: <https://avdc.gsfc.nasa.gov/> (accessed on 5 August 2020)). This is a monthly dataset with 0.5° spatial resolution, calibrated by a set of the FLUXNET 2015 eddy covariance data [48].

Monthly photosynthetic active radiation (PAR) at 1° resolution grid was downloaded from the NASA Langley Research Centre, Cloud and Earth’s Radiant Energy System (CERES, Ed4.1), including adjusted surface PAR both direct and diffuse fluxes under all sky conditions. The total PAR was computed as the sum of both direct and diffuse PAR, and then used to remove the effects of PAR on SIF by normalizing after aggregating into the SIF grid resolution:

$$SIF_{PAR} = \frac{SIF}{PAR} \quad (2)$$

To assess the relationships between vegetation variables and meteor-environmental drivers under drought stress, MODIS daytime land surface temperature (LST, MYD11C3, Collection 6) at monthly scale was included in this study, collected from NASA Earth Observation data (Available online: <https://search.earthdata.nasa.gov> (accessed on 12 August 2020)). Similarly, best quality data remained through eliminating pixels with quality control flag. Global monthly precipitation at 0.1° resolution grid was based on Integrated Multi-Satellite Retrievals for Global Precipitation Measurement (IMERG, Version 6, Final

run, 2007–2019) was collected from NASA Precipitation Processing System (Available online: <https://pps.gsfc.nasa.gov/> (accessed on 12 November 2020)).

2.3. Climate DATA and Land Cover Map

In this study, we utilized monthly the Standardized Precipitation Evapotranspiration Index (SPEI) to characterize the spatial and temporal dynamics of the 2018–2019 extreme drought event across Australia [49]. This dataset at 1° spatial resolution with 1-month, 6-month timescale (indicated as SPEI_{1-month}, SPEI_{6-month}), representing the cumulative water status (deficit or surplus) over the preceding 1 or 6 months respectively, was downloaded from SPEI Global Drought Monitor (Available online: <https://spei.csic.es/> (accessed on 20 July 2020)).

Monthly air temperature (at 2-m height) and soil moisture content (surface 0–7 cm depth, root zone 28–100 cm depth) based on ERA-5 reanalysis data were downloaded from Copernicus Climate Change Service (Available online: <https://cds.climate.copernicus.eu/> (accessed on 28 September 2020)) [50]. Gridded annual potential evapotranspiration (PET) and monthly mean decadal precipitation were collected from the Bureau of Meteorology (Available online: <http://www.bom.gov.au/> (accessed on 5 April 2020)). Firstly, we converted monthly precipitation into annual scale, and then aggregated into 0.1° spatial grid consistent with PET. Secondly, aridity index was computed as annual precipitation normalized by annual PET. The Equation (3) is:

$$AI = \frac{P}{PET} \quad (3)$$

Finally, pixels within the entire study area were binned by AI (every 0.1 increment) into 6 groups from humid to arid region, as shown in Figure 1b.

National Dynamic Land Cover Dataset (DLCD) was used in this research, obtained from Geoscience Australia and Bureau of Agricultural and Resource Economics and Sciences (Available online: <http://www.ga.gov.au/scientific-topics/earth-obs/landcover> (accessed on 10 May 2020)). This dataset validated with abundant field sites was aggregated to 0.5° spatial resolution by most frequent values.

2.4. Eddy Covariance Data

We used five selected flux towers to interpret the satellite-observed dynamic of vegetation under extreme drought. The original level 3 (AU-How, AU-Dry, AU-Step) and level 6 (AU-ASM, AU-TTE) flux data provided by the OzFlux network (Available online: <http://www.ozflux.org.au/> (accessed on 15 July 2020)) were used to pre-process, including quality control assessment, removal of outliers, and gap-filling [51]. The R package, REdDyProc, was implemented for Level 3 data to estimate daily mean GPP with hourly eddy covariance and meteorological data [52]. This tool used the gap-filling and flux partitioning algorithms to partition Level 3 data into GPP and field ecosystem respiration [53], conducted in open-source R scientific computation environment (Version 3.5.1). The estimated daily GPP were aggregated into monthly and 16-day GPP to match with satellite-based observations.

2.5. Analysis

To investigate the responses of dryland vegetation to different drought intensities, we defined two categories of dry conditions based on SPEI_{6-month}, extreme dry (SPEI ≤ −2), and medium dry (−2 < SPEI ≤ −0.5). The R package, GeoRange, was implemented for monthly SPEI data to estimate the total area under extreme dry during the recent two decades (2000–2020). The Mann–Kendall trend test was utilized for time series of the total area and region-wide mean SPEI within the study area. Besides, the statistic (SPEI_{1-month} ≤ −2) was conducted to generate the map of the pixel-wise extreme-dry month during November 2018 to April 2019.

To further examine the response of dryland biomes to extreme drought, we selected four-pair regions of interest (labelled as ROI-1, ROI-2, ROI-3, and ROI-4) distributed from mesic northern to xeric southern areas. The selection criteria are: (1) same or highly similar biome types in each ROI; (2) the sub-regions within ROIs underwent different drought conditions (extreme dry, medium dry, respectively). ROI-1 are mainly covered by woodlands and open woodlands. ROI-2 and ROI-3 are covered by scattered shrubs and grasses. Vegetation in ROI-4 is dominated by Hummock grasses mixed with scattered shrubs. In addition, ROI-2 and ROI-4 were also under extreme dry conditions in the monsoon season of 2012–2013 and 2015–2016, respectively (Figure S1).

With the purpose of detecting drought-related signals by eliminating seasonality, monthly anomalies (ΔX) and standardized anomalies (X_{SA}) of all the aforementioned variables were calculated as a deviation from their corresponding multiyear (2007–2018) mean of each month. The Equations (4) and (5) are:

$$\Delta X = X_m - \overline{X_m} \quad (4)$$

$$X_{SA} = \frac{X_{nm} - \overline{X_m}}{\sigma_m} \quad (5)$$

where n is the yearly temporal coverage from 2007 to 2018, X_{nm} is the monthly ranging from July to June, $\overline{X_m}$ and σ_m are the mean and standard deviation of time series X at month m .

To quantify the relationship between satellite-based observation and tower-based measurement, the coefficient of determination (r^2) was calculated across five selected tower sites at different spatial (0.5° , 0.05°) and temporal (monthly, 16-day) resolutions. All satellite datasets were extracted from a 3×3 window centered on each flux tower site respectively. A t -test was utilized to examine the statistically significant level of the relationships (p -value).

Data processing, analysis, and visualization were conducted in open-source R scientific computation environment (Version 3.6.2) and associated packages contributed by the R user community (Available online: <http://cran.r-project.org> (accessed on 20 August 2020)).

3. Results

3.1. Spatiotemporal Dynamics of the 2018–2019 Extreme Drought

From the start of the new century, there was a significant increase trend in the total area influenced by extreme dry condition and an opposite trend in the region-wide mean SPEI (p -value < 0.0001). The extreme, 4-month drought spanning from December 2018 to March 2019 was the worst drought event during the last two decades over central and northwest Australia (Figure 2), of which almost the entire region was influenced by this event (Figure 3a). During the 2018–2019 monsoon season, a total area of 1.75 million km^2 was under extreme dry condition extending from north to xeric central Australia (15° – 26°S and 118° – 138°E), particularly in December 2018 and January 2019. In addition, the xeric inland experienced a longer extreme dry period (more than 2 months) relative to the mesic northern coastal regions (Figure 3b).

Temporal variations in satellite-based SIF, SIF_{PAR} , EVI, and GPP averaged within the extent of extreme and medium dry, respectively, are displayed in Figure 4. Compared with approximately one standard deviation (SD) decline in all vegetation variables under medium dry, those exhibited 2–3 times SD decrease relative to climatology under extreme situation. Correspondingly, both SIFPAR and EVI showed the largest reduction from January 2019 as a consequence of persistent rainfall deficit as well as increased temperature since November 2018.

Spatial patterns of standardized anomalies of precipitation, surface/root zone soil moisture, LST, SIF, SIF_{PAR} , EVI, and GPP during the 2018–2019 monsoon season are shown in Figure 5, along with the corresponding pixel density classified by extreme and medium dry. Meteorological data show that 87%, 25% of study region appeared rainfall anomalies below than -1 SD, -2 SD, respectively, and 91%, 60% of the area exhibited air temperature

anomalies larger than 1 SD and 2 SD, revealing it was a large-scale drought event coupled with an extreme heatwave (Figure 5a,d). The persistently reduced precipitation along with higher temperature results in depletion of both surface and root zone soil water content over most areas, of which 70%, 50% showed less than -1 SD, respectively (Figure 5b,c).

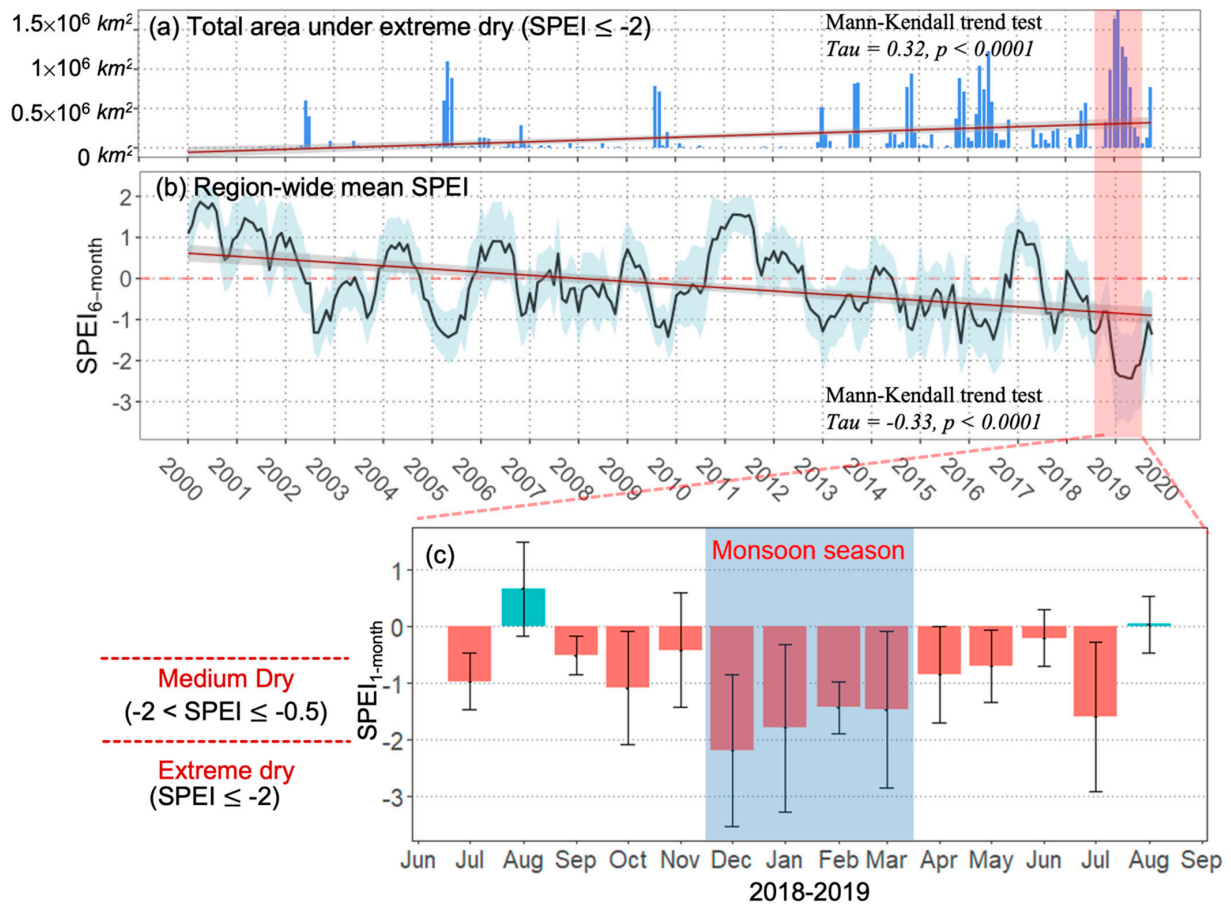


Figure 2. (a) Time series of the total area under extreme dry within the extent of study region during 2000–2019. Red line refers to the linear regression line. (b) Region-wide mean monthly $SPEI_{6\text{-month}}$ during 2000–2019. (c) Region-wide mean monthly $SPEI_{1\text{-month}}$ during 2018–2019.

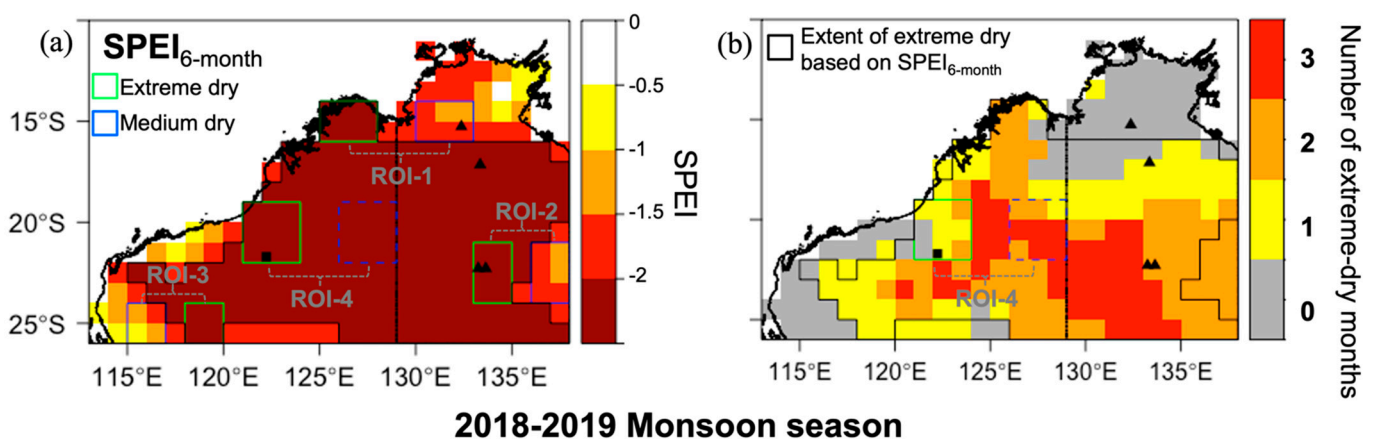


Figure 3. (a) Spatial pattern of drought intensity based on $SPEI_{6\text{-month}}$ during 2018–2019 monsoon season. (b) Pixel-wise number of extreme-dry months based on $SPEI_{1\text{-month}}$. Four pairs of ROIs are shown in Figure 3a. The black boundary represents the extent of extreme (within) and medium (outside) dry.

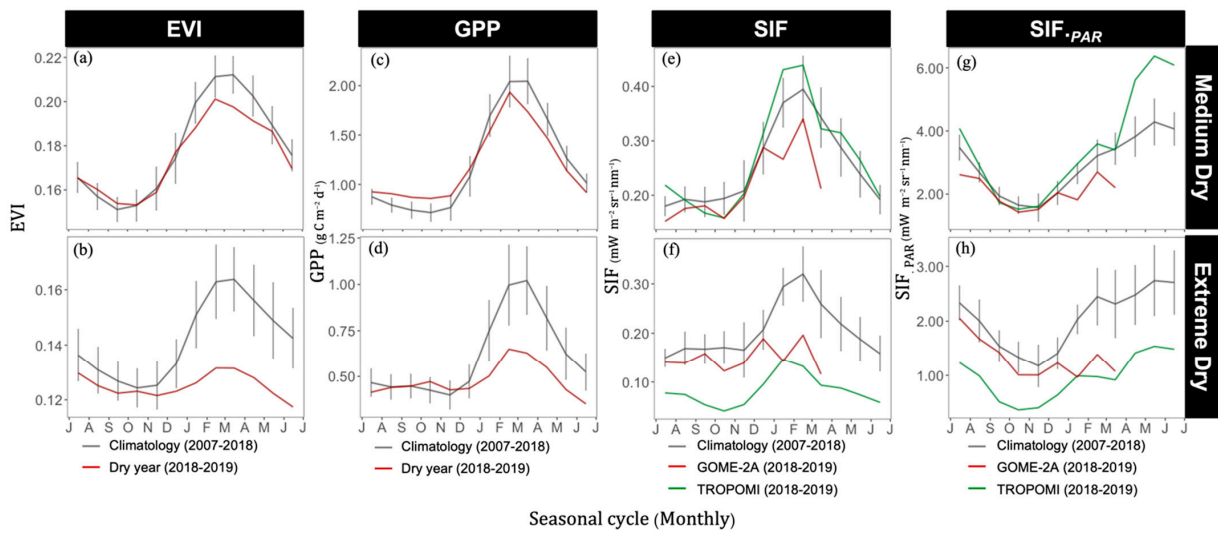


Figure 4. The spatially averaged seasonal cycles of monthly EVI, GPP, SIF, and SIF_{PAR} within (a,c,e,g) medium and (b,d,f,h) extreme dry extent from July 2018 to June 2019. The grey curves represent the monthly multiyear mean (2007–2018). Vertical lines refer to ± 1 standard deviation.

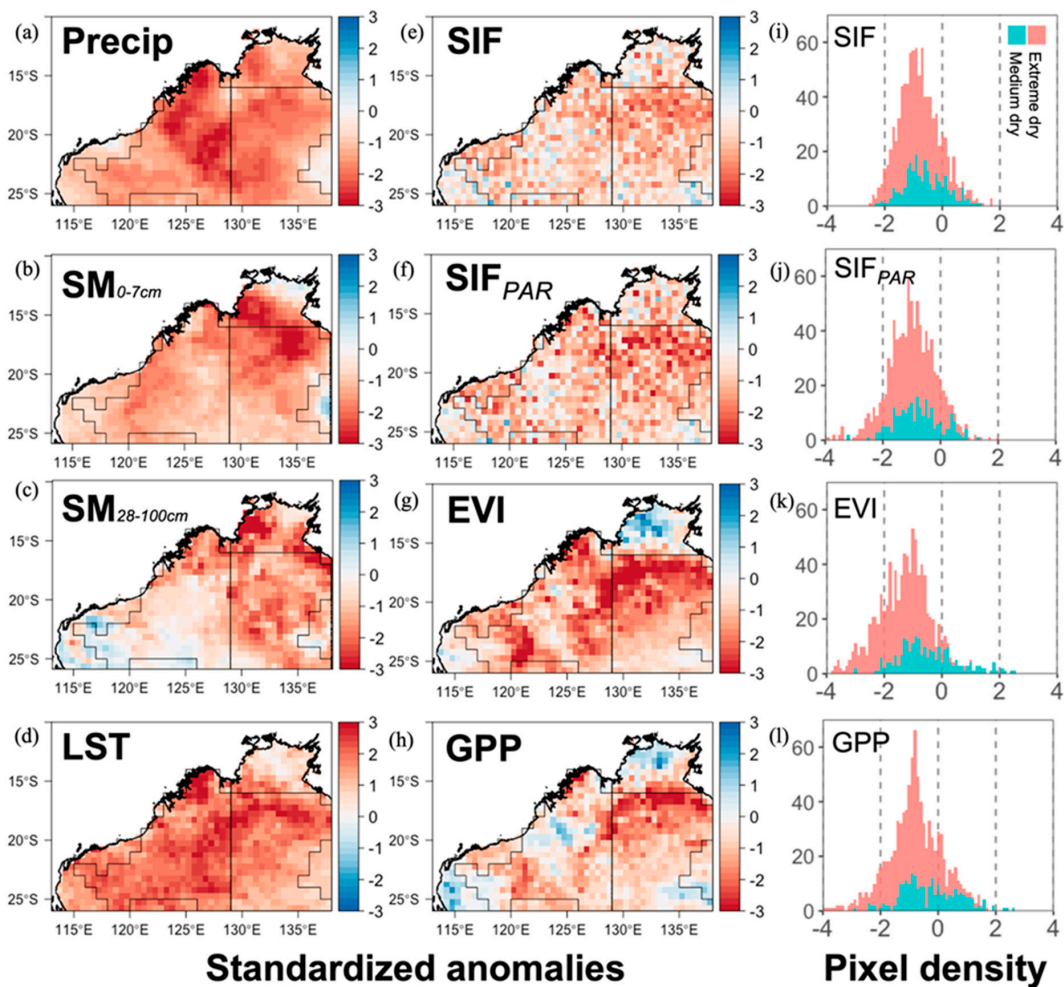


Figure 5. (a–h) Spatial distributions of the standardized anomalies of precipitation, surface/root zone soil moisture, LST, SIF, SIF_{PAR}, EVI, and GPP during 2018–2019 monsoon season. (i–l) Pixel density of four vegetation variables within the extent of extreme and medium dry.

Vegetation growth is largely affected by the extreme drought, and the majority of the area showed negative anomalies for all vegetation variables relative to the multiyear mean (Figure 5e–h). SIF_{PAR} and EVI exhibited a similar spatial pattern, where those were remarkably negative anomalies (< -2 SD) between 17° – 20° S and 129° – 138° E (Figure 5f,g). SIF and SIF_{PAR} showed proportional pixels distribution under extreme dry and medium dry, while there was an obvious distinction for EVI (Figure 5i–k). This discrepancy between SIF and EVI was mainly caused by the divergent responses over northern humid northern Australia (11° – 15° S), where EVI exhibited evidently positive anomalies in comparison to slightly depressed SIF, SIF_{PAR} .

3.2. Responses of Dryland Vegetation to Diverse Drought Intensity

To investigate the response of major biome types of dryland vegetation to different drought intensity, four pairs of ROIs were inter- and intra-compared during 2018–2019 extreme drought as well as associated 2012–2013 and 2015–2016 drought events. Temporal variation in SIF, EVI averaged within ROIs are presented, along with seasonal anomalies of SIF, EVI (Figure 6). There were prominent differences among ROI-1 and ROI-3, of which both SIF and EVI showed larger negative anomalies under extreme dry relative to medium dry (Figure 6a,b,g,h). Within semi-arid ROI-2, both vegetation variables exhibited equivalent magnitude of negative anomalies regardless of drought severity under two contrasting drought events of 2012–2013 and 2018–2019 (Figure 6c–f). Similarly, semi-arid region partially covered with hummock grass (ROI-4), SIF also showed comparably negative anomalies under both extreme and medium dry of 2015–2016 (Figure 6l), while EVI displayed distinct responses (Figure 6k). In addition to the drought intensity, the response of vegetation was also affected by time scales of extreme drought, as evident by ROI-4 in 2018–2019 (Figure 6i,j). We found both sub-regions of ROI-4 were under extreme dry conditions, but with different time scales of extreme-dry period (Figure 3a,b), which leads to the larger reduction of SIF and EVI under longer periods of extreme dry conditions.

3.3. Comparison of SIF and EVI in Response to Drought

To further explore the difference in response of biome-specific vegetation of SIF and EVI to extreme drought, anomalies of SIF and EVI among the entire region under extreme and medium dry are shown in Figure 7. In general, the magnitude of anomalies of SIF and EVI was proportional to the mean SPEI among each category (Figure 7a,d). Tussock grasslands under the worst dry situation in 2018–2019 also exhibited the largest reduction of both SIF and EVI compared with other major biomes (Figure 7b,c). Apart from this, the largest divergent magnitude of anomalies under extreme and medium dry conditions was also shown. Relative to arid/semiarid biomes (e.g., hummock grassland, open shrubland, and scattered shrubs and grasses), mesic ecosystems (e.g., woodland, open woodland) exhibited larger differences under two drought intensities (Figure 7b,c). There was an evident trend for EVI, with the amplified difference between extreme and medium dry from arid to humid climate regimes (Figure 7f), especially for positively anomalous EVI under medium dry ($AI > 0.5$), mainly distributed over northern coastal areas (Figure 5). Conversely, the majority of SIF across different biome types or climate regimes showed negative anomalies with comparable magnitude, regardless of diverse drought intensity (Figure 7b,e).

Temporal percentage of drought-related vegetation decline indicated by EVI and SIF at a monthly and 16-day scale is shown in Figure 8. At the beginning of this drought event (November 2018), approximately 38%, 20% of the area was affected by moderate ($< -0.5\sigma$) and severe ($< -1\sigma$) losses, respectively, indicated by EVI, and increased to over 80%, 50% with the development of extreme drought (Figure 8a). The percentage of moderate and severe reduction observed by SIF, SIF_{PAR} in November of 2018 was around 36%, 18%. In addition, the percentages of affected area revealed by SIF slightly decreased after reaching the peak in February of 2019, while the impacted region indicated by EVI remained growing (Figure 8a–c).

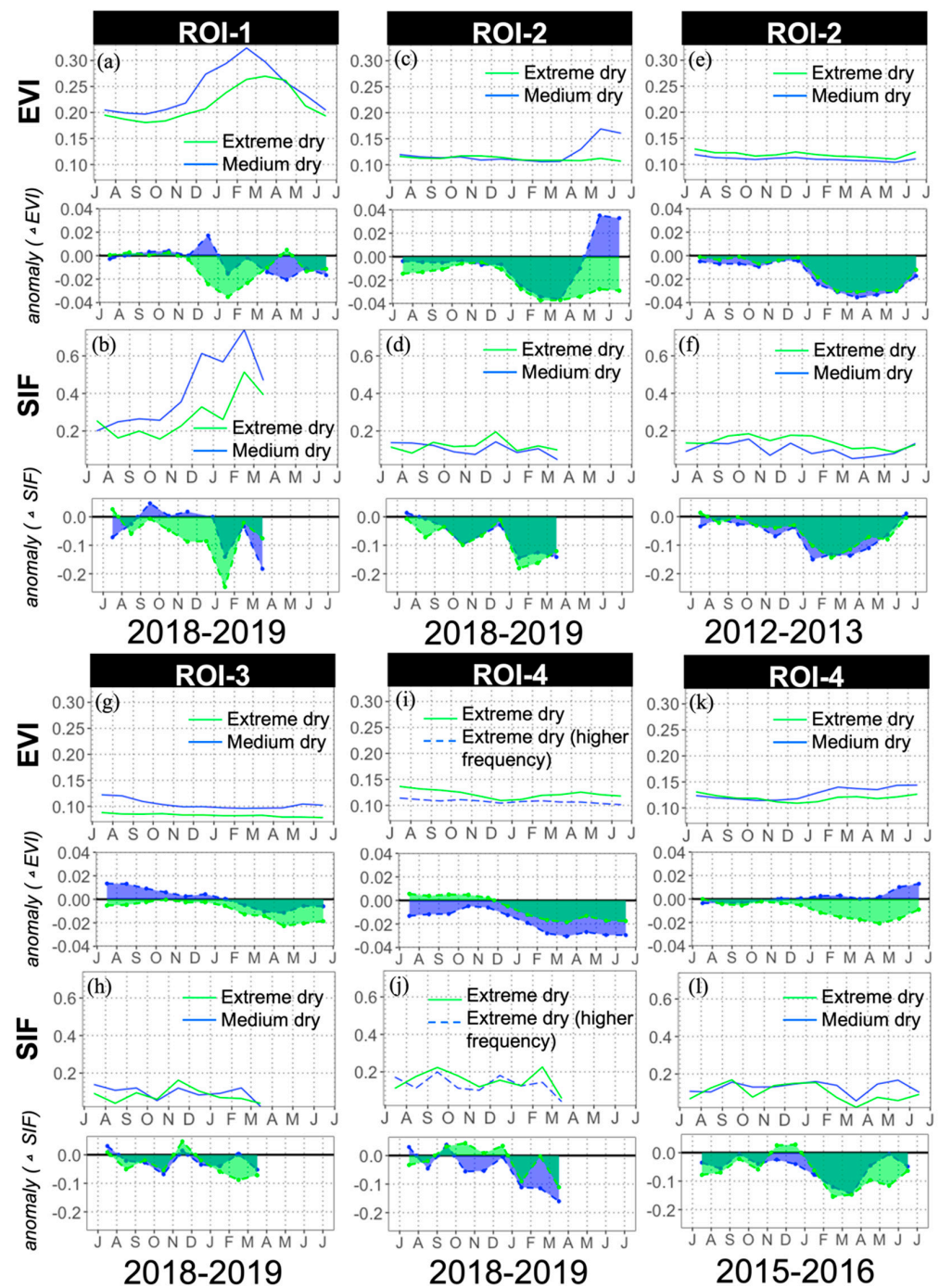


Figure 6. Region-wide seasonal cycles and anomalies of (a,c,g,i) EVI and (b,d,h,j) SIF within four pairs of ROIs in 2018–2019. Seasonal profiles of SIF and EVI within (e,f) ROI–2 in 2012–2013 and (k,l) ROI–4 in 2015–2016. Bottom panels of each figure refer to the anomalies of SIF or EVI relative to climatology (2007–2018).

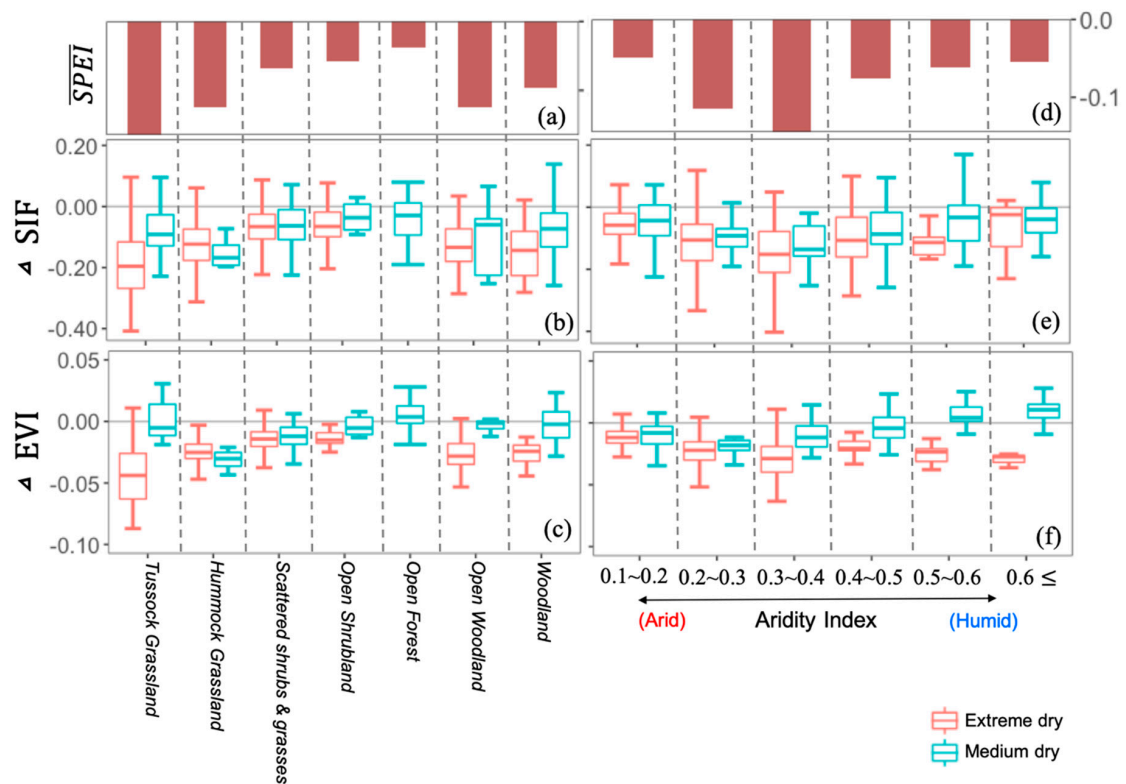


Figure 7. Boxplot of anomalies of EVI and SIF under extreme and medium dry in 2018–2019 grouped by (b,c) major biome types and (e,f) aridity index. (a,d) The top panel refers to the spatially mean SPEI of each category.

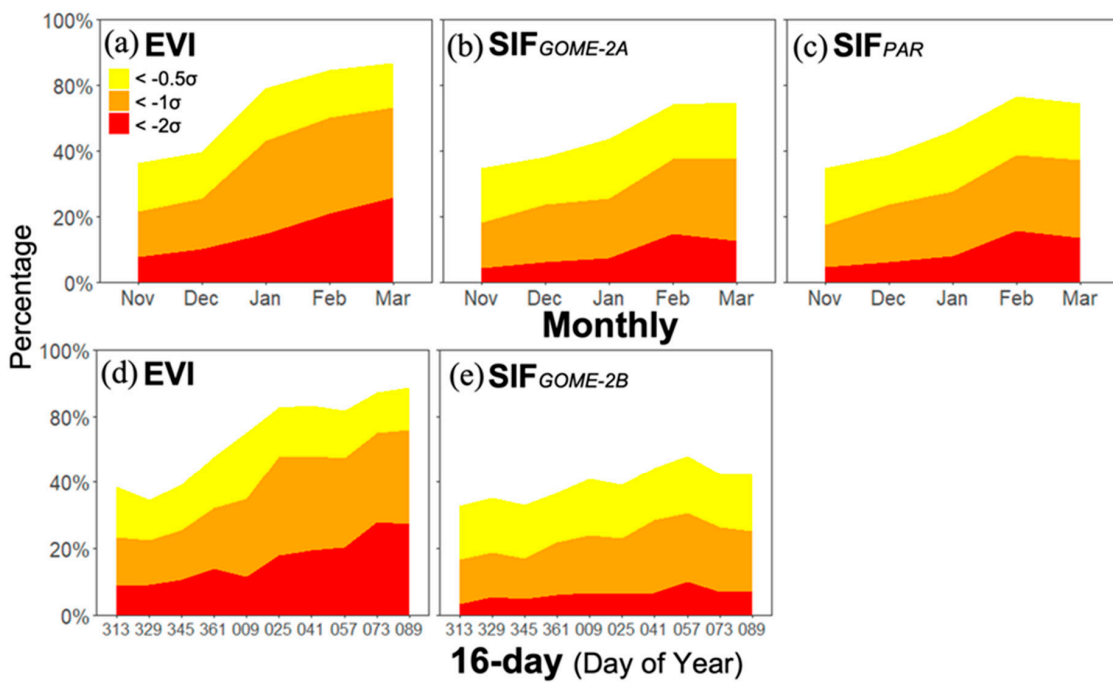


Figure 8. (a,b,c) Monthly and (d,e) 16-day time series of the percentage of drought-induced vegetation reduction indicated by EVI, SIF, and SIF_{PAR} under moderately ($< -0.5\sigma$), severely ($< -1\sigma$), and extremely ($< -2\sigma$) negative anomalies. σ indicates the standard deviation of the monthly SIF, EVI during 2007–2018 as well as 16-day SIF, EVI during 2013–2018. The text of the x-axis in Figure 9d,e refer to the day of year from November 2018 to March 2019.

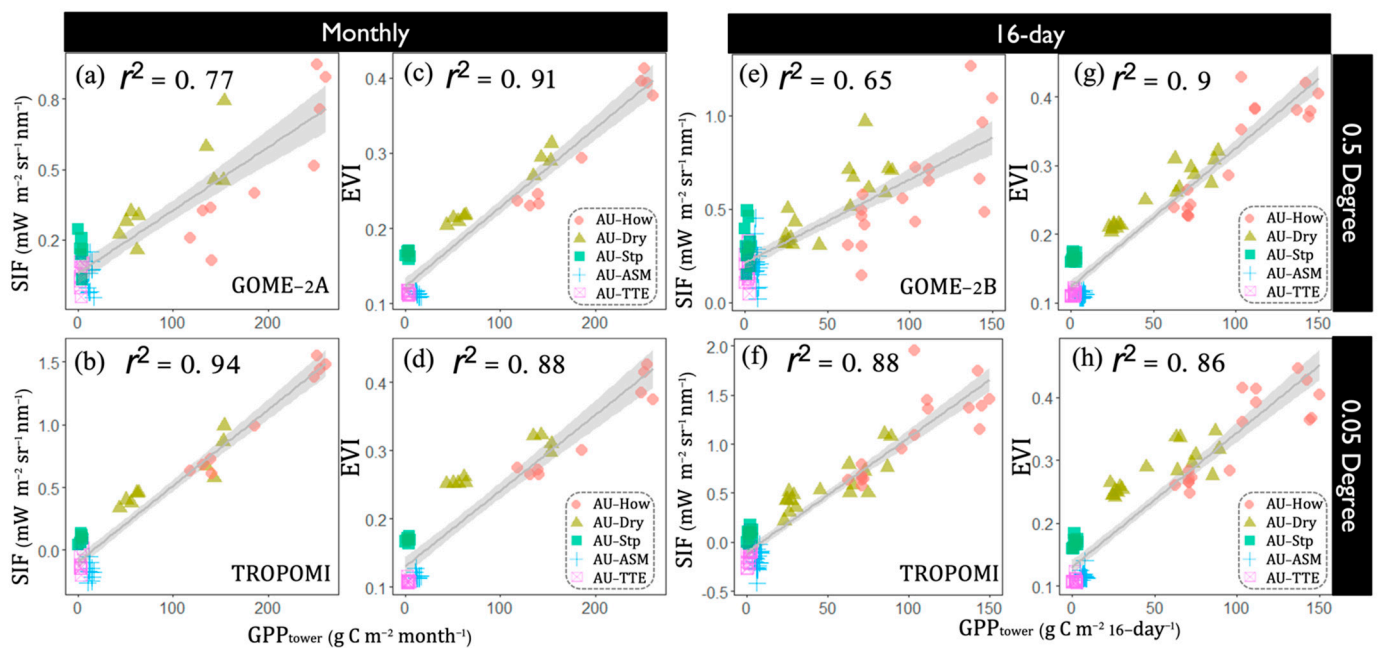


Figure 9. (a–h) Relationship between tower-based GPP and satellite-based SIF, EVI in 2018–2019 across five flux tower sites at different spatial (0.5°, 0.05° grid) and temporal (monthly, 16-day) resolution. The bottom-right embedded box shows the legend of the five flux tower sites. (p value < 0.001).

To further contrast the responses of SIF and EVI at a higher temporal scale, 16-day time series of percentage of moderate/severe/extreme anomalies indicated by EVI and SIF was presented in Figure 8d,e. There was apparently a larger proportion of vegetation decline indicated by EVI than SIF at each category of anomalies, especially over 20% of the area in the middle of March (DOY = 73) which was affected by extreme ($< -2\sigma$) reduction observed by EVI relative to the maximum 7%, indicated by SIF at the end of February (DOY = 57). Besides, the percent of pixels with no seasonality detected by EVI was also higher than that observed by SIF.

3.4. Cross-Comparison with In-Situ Measurements

With the purpose of validating satellite-based observation with field measurement, Figure 9 presents the relationship between tower-based GPP and satellite-based SIF, EVI in 2018–2019 across five selected sites at different spatial and temporal resolutions. Despite diverse spatiotemporal resolution, both satellite-observed SIF, EVI were overall significantly (p -value < 0.001) associated with in-situ measurement GPP (r^2 ranging from 0.65 to 0.94) in the extremely dry year of 2018–2019. There was an enhanced correspondence between GPP and SIF with increasing spatial resolution (from 0.5° to 0.05° grid) for both monthly and 16-day temporal scales (Figure 9a,b,e,f). Besides, we found a stronger relationship between field measurement and satellite-based observation at monthly series ($r^2 = 0.77, 0.94$) relative to 16-day series ($r^2 = 0.65, 0.88$). The close correlation between GPP and EVI remained across different spatial and temporal resolution (r^2 ranging from 0.86 to 0.91, Figure 9c,d,g,h). For three southern sites (AU-Stp, AU-ASM, AU-TTE) that suffered from extreme dryness in 2018–2019 there was large reduction, and seasonal amplitude was barely detected by either in-situ measurement or satellite observation (EVI).

4. Discussion

4.1. Potential of Spaceborne SIF for Drought Monitoring over Water-Limited Ecosystems

Satellite-based SIF observations capture the spatial and temporal variations in dryland vegetation under 2018–2019 extreme drought in Australia (Figures 4 and 5). Relative

to EVI and GPP, the fluctuated SIF series and notable spatial speckling were probably due to high retrieval noise in sparsely vegetated regions [54], especially for lower signal levels under extreme drought. Overall, SIF and EVI exhibited resemblance to spatial and temporal responses of dryland vegetation to this extreme event, wherein the central study area (between 17–20°S and 129–138°E) showed the most remarkable reduction (Figure 5). The primary difference in spatial dynamics of two variables occurred over the northern humid region (between 12–15°S and 129–138°E) under medium drought, where SIF showed marginally negative anomalies in comparison to positive EVI anomalies (Figure 5). This is consistent with previous studies [32,34,36,55], revealing that there was a considerable decoupling of photosynthesis and greenness dynamics under moderate dry conditions over mesic ecosystems (e.g., forests and woodlands).

Nonetheless, there was concurrently substantial loss in both SIF and EVI over arid and semiarid biome types, and those suffered from extreme rainfall deficit as well as severe heat wave (Figure 5). In particular, a higher percentage of the area indicated by EVI was affected by extreme ($< -2\sigma$) losses than that by SIF throughout the entire 2018–2019 monsoon season (Figures 5 and 8). This finding was against a similar study [38], which concludes satellite SIF observations are more sensitive to water and heat stress than EVI over arid central Australia in the 2019 heatwave. However, the divergent results were primarily ascribed to the different methods to define the anomaly, and they utilized the relative anomaly (a departure from the climatology and divided by the multiyear mean) instead of the standardized anomaly used in this study. The larger variation in magnitude of SIF than that of greenness-based VIs gave rise to the sharper reduction in SIF, indicated by relative anomaly relative to EVI. In addition, insufficient baseline years (2015–2018) in their study may induce more uncertainties as a consequence of highly dynamic climate regime over inland Australia.

On the contrary, we contrasted the responses of two sources of SIF data derived from GOME-2A and GOME-2B with MODIS EVI under two reference climatologies (2007–2018 and 2014–2018), respectively. We found that the percentage of the drought-affected area captured by EVI was consistently higher than that of SIF regardless of diverse temporal scales (Figure 8). The reason for the more significantly negative standardized anomalies of EVI relative to those of SIF was possibly owing to the fact that the dramatically drought-induced reduction in vegetation leads to barely increased magnitude of seasonal cycles over the vast inland area (Figure 9). Apart from this, high-retrieval noise provokes the larger variability of SIF signal over arid/semiarid ecosystems.

Compared with coarse SIF data derived from GOME-2, the state-of-the-art TROPOMI SIF observation with substantially improved spatiotemporal resolution shows an enhanced correlation with tower-based GPP in the extremely dry year of 2018–2019 (Figure 9), implying that this advanced dataset has promising potential for drought monitoring over heterogeneous arid and semiarid ecosystems. As opposed to the fluctuated temporal series and spatial speckling of GOME-2 SIF signal (Figures 4–6 and 9), SIF retrieved from remarkable radiometric performance of TROPOMI exhibits more spatial and temporal consistency, representing a step change in SIF remote sensing capabilities [26,56]. It is worth noting that an abundance of negative values of TROPOMI SIF was observed over central Australia in 2018–2019, probably owing to the retrieval noise. Köhler et al. [26] suggested that negative SIF values mainly occur for single TROPOMI measurements, which should not be over-interpreted. A comprehensive assessment of the capability of the novel dataset over dryland ecosystem needs to be conducted in the future.

4.2. Dynamics of Dryland Vegetation under Different Drought Scenarios

Varying responses of major biome types of dryland vegetation to different drought severity (extreme dry vs medium dry) were observed (Figures 6 and 7). We found enhanced magnitude of reduction of both SIF and EVI in conjunction with increasing drought severity over humid/sub-humid biomes (e.g., forest, woodland, and tussock grasslands). By contrast, the two vegetation variables of arid/semiarid vegetation (e.g., hummock

grasslands, open shrublands) showed comparable losses under extreme and medium dry condition, indicating the largest sensitivity and vulnerability of semiarid ecosystems to the hydroclimatic variations [18,57]. It is not only evident by the 2018–2019 extreme drought, but also the 2012–2013, 2015–2016 drought events in central Australia (Figure 6e–l). As prolonged drought is projected to increase both its frequency and intensity [58,59], drylands will have a more critical role in regulating the global carbon and water cycle [60,61].

Given that the coarse spatial grid (0.5°) induced uncertainty of biome-specific analysis over heterogeneous drylands, re-grouped pixels based on aridity index were used to investigate the responses to the extreme drought at different time scales (Figure 7). As opposed to notably depressed SIF over mesic ecosystem ($AI > 0.6$), EVI remained positive anomalies even under one-month extreme dryness, in line with reported studies concerning dry-season greening of forests [62,63]. Despite that, canopy greenness of humid ecosystems exhibited a significant reduction when the extreme-dry period exceeded one month (≥ 2). Likewise, we found larger magnitudes of decline in arid regions ($AI < 0.3$) resulting from the increasing extreme-dry months, although both sub-regions of ROI-4 suffered from extreme dryness in 2018–2019 (Figure 3a,b, Figures 6l–n and 7). In contrast, both SIF and EVI in semiarid regions ($AI: 0.3\text{--}0.4$) exhibited the largest reduction under short timescales (extreme-dry month ≤ 1), confirming semiarid biomes are the most susceptible to extreme drought.

5. Conclusions

In summary, we investigated the spatial and temporal responses of SIF and EVI of dryland vegetation to the 2018–2019 extreme drought over Australia using multi-source satellite-based SIF observations. In contrast to the enhanced magnitude of reduction of both SIF and EVI in conjunction with increasing drought severity over humid/sub-humid biomes, the two vegetation variables of arid/semiarid vegetation showed comparable negative anomalies regardless of extreme or medium dry conditions, indicating the largest sensitivity and vulnerability of semiarid ecosystems to the hydroclimatic variations. At a 16-day interval, both satellite-based indicators (SIF and EVI) can synchronously detect the impact of extreme drought on dryland vegetation growth. Besides, we find that space-borne SIF is capable of characterizing the spatiotemporal dynamics of drought over water-limited ecosystems despite high retrieval noises, as compared with EVI. The unprecedented SIF derived from TROPOMI shows remarkably enhanced agreement with tower-based GPP in the dry year of 2018–2019, demonstrating the great potential of the advanced dataset to track the dynamics of dryland vegetation under future changing climates. In addition, semiarid ecosystems exhibiting the largest reduction, regardless of drought severity and time scales, are the most sensitive to climatic extremes.

Supplementary Materials: The following supporting information can be downloaded at: <https://www.mdpi.com/article/10.3390/rs14071581/s1>, Figure S1: Spatial pattern of drought intensity based on $SPEI_{6\text{-month}}$ during 2018–2019, 2015–2016, and 2012–2013 monsoon season. Green and blue rectangles refer to the region of interest (ROI). Black triangles refer to five flux tower sites.

Author Contributions: Conceptualization, S.L. and A.H.; methodology, S.L.; validation, S.L.; formal analysis, S.L.; investigation, S.L.; data curation, S.L., S.G. and J.C.; writing—original draft preparation, S.L.; writing—review and editing, A.H., Q.Y., X.M., J.Q., R.Z. and Q.W.; visualization, S.L. and Q.W.; supervision, A.H. and Q.Y.; funding acquisition, Q.W. All authors have read and agreed to the published version of the manuscript.

Funding: This research was funded by the Natural Science Foundation of Fujian Province (2021J01627) and the National Natural Science Foundation of China (41601562).

Institutional Review Board Statement: Not applicable.

Informed Consent Statement: Not applicable.

Data Availability Statement: All satellite-based data well as other datasets in this study are available from the corresponding author upon reasonable request.

Acknowledgments: This work was supported by the Natural Science Foundation of Fujian Province (2021J01627) and the National Natural Science Foundation of China (No. 41601562) for funding this work. The first author acknowledges the financial support from Chinese Scholarship Council, Ministry of Education, China. We also would like to thank the opening of flux tower data for public access by the Australian Terrestrial Ecosystem Research Network (TERN, Available online: www.tern.org.au (accessed on 30 June 2020))—OzFlux facility (Available online: www.ozflux.org.au (accessed on 30 June 2020)).

Conflicts of Interest: The authors declare no conflict of interest.

References

- Jiao, W.; Chang, Q.; Wang, L. The Sensitivity of Satellite Solar-Induced Chlorophyll Fluorescence to Meteorological Drought. *Earth's Future* **2019**, *7*, 558–573.
- Cataldo, E.; Salvi, L.; Mattii, G.B. Effects of Irrigation on Ecophysiology, Sugar Content and thiol Precursors (3-S-Cysteinyllhexan-1-Ol and 3-S-Glutathionylhexan-1-Ol) on Vitis Vinifera Cv. Sauvignon Blanc. *Plant Physiol. Biochem.* **2021**, *164*, 247–259. [[CrossRef](#)] [[PubMed](#)]
- Cataldo, E.; Fucile, M.; Mattii, G.B. A Review: Soil Management, Sustainable Strategies and Approaches to Improve the Quality of Modern Viticulture. *Agronomy* **2021**, *11*, 2359. [[CrossRef](#)]
- Ma, X.; Huete, A.; Cleverly, J.; Eamus, D.; Chevallier, F.; Joiner, J.; Poulter, B.; Zhang, Y.; Guanter, L.; Meyer, W.; et al. Drought Rapidly Diminishes the Large Net CO₂ Uptake in 2011 over Semi-Arid Australia. *Sci. Rep.* **2016**, *6*, 37747. [[CrossRef](#)]
- van Dijk, A.I.J.M.; Beck, H.E.; Crosbie, R.S.; de Jeu, R.A.M.; Liu, Y.Y.; Podger, G.M.; Timbal, B.; Viney, N.R. The Millennium Drought in Southeast Australia (2001–2009): Natural and Human Causes and Implications for Water Resources, Ecosystems, Economy, and Society. *Water Resour. Res.* **2013**, *49*, 1040–1057.
- Haverd, V.; Ahlstrom, A.; Smith, B.; Canadell, J.G. Carbon Cycle Responses of Semi-Arid Ecosystems to Positive Asymmetry in Rainfall. *Glob. Chang. Biol.* **2017**, *23*, 793–800. [[CrossRef](#)]
- Xie, Z.; Huete, A.; Cleverly, J.; Phinn, S.; McDonald-Madden, E.; Cao, Y.; Qin, F. Multi-Climate Mode Interactions Drive Hydrological and Vegetation Responses to Hydroclimatic Extremes in Australia. *Remote Sens. Environ.* **2019**, *231*, 111270. [[CrossRef](#)]
- Broich, M.; Tulbure, M.G.; Verbesselt, J.; Xin, Q.; Wearne, J. Quantifying Australia's Dryland Vegetation Response to Flooding and Drought at Sub-Continental Scale. *Remote Sens. Environ.* **2018**, *212*, 60–78. [[CrossRef](#)]
- Wang, J.; Ding, J.; Yu, D.; Teng, D.; He, B.; Chen, X.; Ge, X.; Zhang, Z.; Wang, Y.; Yang, X.; et al. Machine Learning-Based Detection of Soil Salinity in an Arid Desert Region, Northwest China: A Comparison between Landsat-8 OLI and Sentinel-2 MSI. *Sci. Total Environ.* **2020**, *707*, 136092. [[CrossRef](#)]
- Wang, J.; Ding, J.; Li, G.; Liang, J.; Yu, D.; Aishan, T.; Zhang, F.; Yang, J.; Abulimiti, A.; Liu, J. Dynamic Detection of Water Surface Area of Ebinur Lake Using Multi-Source Satellite Data (Landsat and Sentinel-1A) and Its Responses to Changing Environment. *CATENA* **2019**, *177*, 189–201. [[CrossRef](#)]
- Zhang, J.; Ding, J.; Wu, P.; Tan, J.; Huang, S.; Teng, D.; Cao, X.; Wang, J.; Chen, W. Assessing Arid Inland Lake Watershed Area and Vegetation Response to Multiple Temporal Scales of Drought Across the Ebinur Lake Watershed. *Sci. Rep.* **2020**, *10*, 1354. [[CrossRef](#)] [[PubMed](#)]
- Huete, A.R.; Restrepo-Coupe, N.; Ratana, P.; Didan, K.; Saleska, S.R.; Ichii, K.; Panuthai, S.; Gamo, M. Multiple Site Tower Flux and Remote Sensing Comparisons of Tropical Forest Dynamics in Monsoon Asia. *Agric. For. Meteorol.* **2008**, *148*, 748–760. [[CrossRef](#)]
- Kath, J.; le Brocque, A.F.; Reardon-Smith, K.; Apan, A. Remotely Sensed Agricultural Grassland Productivity Responses to Land Use and Hydro-Climatic Drivers under Extreme Drought and Rainfall. *Agric. For. Meteorol.* **2019**, *268*, 11–22. [[CrossRef](#)]
- Wang, Q.; Yang, Y.; Liu, Y.; Tong, L.; Zhang, Q.; Li, J. Assessing the Impacts of Drought on Grassland Net Primary Production at the Global Scale. *Sci. Rep.* **2019**, *9*, 14041. [[PubMed](#)]
- Xu, H.; Wang, X.; Zhao, C.; Yang, X. Diverse Responses of Vegetation Growth to Meteorological Drought across Climate Zones and Land Biomes in Northern China from 1981 to 2014. *Agric. For. Meteorol.* **2018**, *262*, 1–13. [[CrossRef](#)]
- Zeng, J.; Zhang, R.; Qu, Y.; Bento, V.A.; Zhou, T.; Lin, Y.; Wu, X.; Qi, J.; Shui, W.; Wang, Q. Improving the Drought Monitoring Capability of VHI at the Global Scale via Ensemble Indices for Various Vegetation Types from 2001 to 2018. *Weather Clim. Extrem.* **2022**, *35*, 100412. [[CrossRef](#)]
- Zhang, R.; Wu, X.; Zhou, X.; Ren, B.; Zeng, J.; Wang, Q. Investigating the Effect of Improved Drought Events Extraction Method on Spatiotemporal Characteristics of Drought. *Theor. Appl. Climatol.* **2022**, *147*, 395–408. [[CrossRef](#)]
- Ma, X.; Huete, A.; Moran, S.; Ponce-Campos, G.; Eamus, D. Abrupt Shifts in Phenology and Vegetation Productivity under Climate Extremes. *J. Geophys. Res. Biogeosci.* **2015**, *120*, 2036–2052. [[CrossRef](#)]
- Wang, Q.; Qi, J.; Qiu, H.; Li, J.; Cole, J.; Waldhoff, S.; Zhang, X. Pronounced Increases in Future Soil Erosion and Sediment Deposition as Influenced by Freeze–Thaw Cycles in the Upper Mississippi River Basin. *Environ. Sci. Technol.* **2021**, *55*, 9905–9915. [[CrossRef](#)]

20. Sun, Y.; Fu, R.; Dickinson, R.; Joiner, J.; Frankenberg, C.; Gu, L.; Xia, Y.; Fernando, N. Drought Onset Mechanisms Revealed by Satellite Solar-Induced Chlorophyll Fluorescence: Insights from Two Contrasting Extreme Events. *J. Geophys. Res. Biogeosci.* **2015**, *120*, 2427–2440. [[CrossRef](#)]
21. Frankenberg, C.; Fisher, J.B.; Worden, J.; Badgley, G.; Saatchi, S.S.; Lee, J.; Toon, G.C.; Butz, A.; Jung, M.; Kuze, A. New Global Observations of the Terrestrial Carbon Cycle from GOSAT: Patterns of Plant Fluorescence with Gross Primary Productivity. *Geophys. Res. Lett.* **2011**, *38*, L17706.
22. Guan, K.; Pan, M.; Li, H.; Wolf, A.; Wu, J.; Medvigy, D.; Caylor, K.K.; Sheffield, J.; Wood, E.F.; Malhi, Y.; et al. Photosynthetic Seasonality of Global Tropical Forests Constrained by Hydroclimate. *Nat. Geosci.* **2015**, *8*, 284–289. [[CrossRef](#)]
23. Sun, Y.; Frankenberg, C.; Wood, J.D.; Schimel, D.S.; Jung, M.; Guanter, L.; Drewry, D.T.; Verma, M.; Porcar-Castell, A.; Griffis, T.J. OCO-2 Advances Photosynthesis Observation from Space via Solar-Induced Chlorophyll Fluorescence. *Science* **2017**, *358*, 713–728.
24. Guan, K.; Berry, J.A.; Zhang, Y.; Joiner, J.; Guanter, L.; Badgley, G.; Lobell, D.B. Improving the Monitoring of Crop Productivity Using Spaceborne Solar-Induced Fluorescence. *Glob. Chang. Biol.* **2016**, *22*, 716–726. [[CrossRef](#)]
25. Kira, O.; Sun, Y. Extraction of Sub-Pixel C3/C4 Emissions of Solar-Induced Chlorophyll Fluorescence (SIF) Using Artificial Neural Network. *ISPRS J. Photogramm. Remote Sens.* **2020**, *161*, 135–146.
26. Köhler, P.; Frankenberg, C.; Magney, T.S.; Guanter, L.; Joiner, J.; Landgraf, J. Global Retrievals of Solar-induced Chlorophyll Fluorescence with TROPOMI: First Results and Intersensor Comparison to OCO-2. *Geophys. Res. Lett.* **2018**, *45*, 10–456.
27. Yang, X.; Tang, J.; Mustard, J.F.; Lee, J.-E.; Rossini, M.; Joiner, J.; Munger, J.W.; Kornfeld, A.; Richardson, A.D. Solar-Induced Chlorophyll Fluorescence That Correlates with Canopy Photosynthesis on Diurnal and Seasonal Scales in a Temperate Deciduous Forest. *Geophys. Res. Lett.* **2015**, *42*, 2977–2987. [[CrossRef](#)]
28. Biederman, J.A.; Scott, R.L.; Bell, T.W.; Bowling, D.R.; Dore, S.; Garatuza-Payan, J.; Kolb, T.E.; Krishnan, P.; Krofcheck, D.J.; Litvak, M.E. CO₂ Exchange and Evapotranspiration across Dryland Ecosystems of Southwestern North America. *Glob. Chang. Biol.* **2017**, *23*, 4204–4221.
29. Guanter, L.; Zhang, Y.; Jung, M.; Joiner, J.; Voigt, M.; Berry, J.A.; Frankenberg, C.; Huete, A.R.; Zarco-Tejada, P.; Lee, J.-E. Global and Time-Resolved Monitoring of Crop Photosynthesis with Chlorophyll Fluorescence. *Proc. Natl. Acad. Sci. USA* **2014**, *111*, E1327–E1333.
30. Short Gianotti, D.J.; Rigden, A.J.; Salvucci, G.D.; Entekhabi, D. Satellite and Station Observations Demonstrate Water Availability's Effect on Continental-scale Evaporative and Photosynthetic Land Surface Dynamics. *Water Resour. Res.* **2019**, *55*, 540–554.
31. Song, L.; Guanter, L.; Guan, K.; You, L.; Huete, A.; Ju, W.; Zhang, Y. Satellite Sun-induced Chlorophyll Fluorescence Detects Early Response of Winter Wheat to Heat Stress in the Indian Indo-Gangetic Plains. *Glob. Chang. Biol.* **2018**, *24*, 4023–4037. [[PubMed](#)]
32. Zhang, L.; Qiao, N.; Huang, C.; Wang, S. Monitoring Drought Effects on Vegetation Productivity Using Satellite Solar-Induced Chlorophyll Fluorescence. *Remote Sens.* **2019**, *11*, 378.
33. Qian, X.; Qiu, B.; Zhang, Y. Widespread Decline in Vegetation Photosynthesis in Southeast Asia Due to the Prolonged Drought During the 2015/2016 El Niño. *Remote Sens.* **2019**, *11*, 910.
34. Wang, X.; Wang, T.; Liu, D.; Zhang, T.; Xu, J.; Cui, G.; Lv, G.; Huang, H. Multisatellite Analyses of Spatiotemporal Variability in Photosynthetic Activity Over the Tibetan Plateau. *J. Geophys. Res. Biogeosci.* **2019**, *124*, 3778–3797.
35. Wang, X.; Qiu, B.; Li, W.; Zhang, Q. Impacts of Drought and Heatwave on the Terrestrial Ecosystem in China as Revealed by Satellite Solar-Induced Chlorophyll Fluorescence. *Sci. Total Environ.* **2019**, *693*, 133627.
36. Yang, J.; Tian, H.; Pan, S.; Chen, G.; Zhang, B.; Dangal, S. Amazon Drought and Forest Response: Largely Reduced Forest Photosynthesis but Slightly Increased Canopy Greenness during the Extreme Drought of 2015/2016. *Glob. Chang. Biol.* **2018**, *24*, 1919–1934. [[CrossRef](#)]
37. Walther, S.; Duveiller, G.; Jung, M.; Guanter, L.; Cescatti, A.; Camps-Valls, G. Satellite Observations of the Contrasting Response of Trees and Grasses to Variations in Water Availability. *Geophys. Res. Lett.* **2019**, *46*, 1429–1440.
38. Qiu, B.; Ge, J.; Guo, W.; Pitman, A.J.; Mu, M. Responses of Australian Dryland Vegetation to the 2019 Heatwave at a Sub-daily Scale. *Geophys. Res. Lett.* **2020**, *47*, e2019GL086569.
39. Doughty, R.; Köhler, P.; Frankenberg, C.; Magney, T.S.; Xiao, X.; Qin, Y.; Wu, X.; Moore, B. TROPOMI Reveals Dry-Season Increase of Solar-Induced Chlorophyll Fluorescence in the Amazon Forest. *Proc. Natl. Acad. Sci. USA* **2019**, *116*, 22393–22398.
40. Vicente-Serrano, S.M.; Gouveia, C.; Camarero, J.J.; Beguería, S.; Trigo, R.; López-Moreno, J.I.; Azorín-Molina, C.; Pasho, E.; Lorenzo-Lacruz, J.; Revuelto, J. Response of Vegetation to Drought Time-Scales across Global Land Biomes. *Proc. Natl. Acad. Sci. USA* **2013**, *110*, 52–57.
41. Peña-Gallardo, M.; Vicente-Serrano, S.M.; Quiring, S.; Svoboda, M.; Hannaford, J.; Tomas-Burguera, M.; Martín-Hernández, N.; Domínguez-Castro, F.; el Kenawy, A. Response of Crop Yield to Different Time-Scales of Drought in the United States: Spatio-Temporal Patterns and Climatic and Environmental Drivers. *Agric. For. Meteorol.* **2019**, *264*, 40–55. [[CrossRef](#)]
42. Ma, X.; Huete, A.; Yu, Q.; Coupe, N.R.; Davies, K.; Broich, M.; Ratana, P.; Beringer, J.; Hutley, L.B.; Cleverly, J. Spatial Patterns and Temporal Dynamics in Savanna Vegetation Phenology across the North Australian Tropical Transect. *Remote Sens. Environ.* **2013**, *139*, 97–115.
43. Beringer, J.; Hutley, L.B.; McHugh, I.; Arndt, S.K.; Campbell, D.; Cleugh, H.A.; Cleverly, J.; de Dios, V.R.; Eamus, D.; Evans, B. An Introduction to the Australian and New Zealand Flux Tower Network-OzFlux. *Biogeosciences* **2016**, *13*, 5895–5916.

44. Joiner, J.; Yoshida, Y.; Vasilkov, A.P.; Schaefer, K.; Jung, M.; Guanter, L.; Zhang, Y.; Garrity, S.; Middleton, E.M.; Huemmrich, K.F.; et al. The Seasonal Cycle of Satellite Chlorophyll Fluorescence Observations and Its Relationship to Vegetation Phenology and Ecosystem Atmosphere Carbon Exchange. *Remote Sens. Environ.* **2014**, *152*, 375–391. [[CrossRef](#)]
45. Huete, A.; Didan, K.; Miura, T.; Rodriguez, E.P.; Gao, X.; Ferreira, L.G. Overview of the Radiometric and Biophysical Performance of the MODIS Vegetation Indices. *Remote Sens. Environ.* **2002**, *83*, 195–213.
46. Wang, J.; Hu, X.; Shi, T.; He, L.; Hu, W.; Wu, G. Assessing Toxic Metal Chromium in the Soil in Coal Mining Areas via Proximal Sensing: Prerequisites for Land Rehabilitation and Sustainable Development. *Geoderma* **2022**, *405*, 115399. [[CrossRef](#)]
47. Wang, J.; Ding, J.; Yu, D.; Ma, X.; Zhang, Z.; Ge, X.; Teng, D.; Li, X.; Liang, J.; Lizaga, I.; et al. Capability of Sentinel-2 MSI Data for Monitoring and Mapping of Soil Salinity in Dry and Wet Seasons in the Ebinur Lake Region, Xinjiang, China. *Geoderma* **2019**, *353*, 172–187. [[CrossRef](#)]
48. Joiner, J.; Yoshida, Y.; Zhang, Y.; Duveiller, G.; Jung, M.; Lyapustin, A.; Wang, Y.; Tucker, C.J. Estimation of Terrestrial Global Gross Primary Production (GPP) with Satellite Data-Driven Models and Eddy Covariance Flux Data. *Remote Sens.* **2018**, *10*, 1346.
49. Wang, Q.; Zeng, J.; Qi, J.; Zhang, X.; Zeng, Y.; Shui, W.; Xu, Z.; Zhang, R.; Wu, X.; Cong, J. A Multi-Scale Daily SPEI Dataset for Drought Characterization at Observation Stations over Mainland China from 1961 to 2018. *Earth Syst. Sci. Data* **2021**, *13*, 331–341. [[CrossRef](#)]
50. Zhang, W.; Zhang, B.; Zhu, W.; Tang, X.; Li, F.; Liu, X.; Yu, Q. Comprehensive Assessment of MODIS-Derived near-Surface Air Temperature Using Wide Elevation-Spanned Measurements in China. *Sci. Total Environ.* **2021**, *800*, 149535. [[CrossRef](#)]
51. Cleverly, J.; Chen, C.; Boulain, N.; Villalobos-Vega, R.; Faux, R.; Grant, N.; Yu, Q.; Eamus, D. Aerodynamic Resistance and Penman–Monteith Evapotranspiration over a Seasonally Two-Layered Canopy in Semiarid Central Australia. *J. Hydrometeorol.* **2013**, *14*, 1562–1570. [[CrossRef](#)]
52. Wutzler, T.; Lucas-Moffat, A.; Migliavacca, M.; Knauer, J.; Sickel, K.; Šigut, L.; Menzer, O.; Reichstein, M. Basic and Extensible Post-Processing of Eddy Covariance Flux Data with REddyProc. *Biogeosciences* **2018**, *15*, 5015–5030.
53. Reichstein, M.; Falge, E.; Baldocchi, D.; Papale, D.; Aubinet, M.; Berbigier, P.; Bernhofer, C.; Buchmann, N.; Gilmanov, T.; Granier, A. On the Separation of Net Ecosystem Exchange into Assimilation and Ecosystem Respiration: Review and Improved Algorithm. *Glob. Chang. Biol.* **2005**, *11*, 1424–1439.
54. Geruo, A.; Velicogna, I.; Kimball, J.S.; Du, J.; Kim, Y.; Colliander, A.; Njoku, E. Satellite-Observed Changes in Vegetation Sensitivities to Surface Soil Moisture and Total Water Storage Variations since the 2011 Texas Drought. *Environ. Res. Lett.* **2017**, *12*, 054006. [[CrossRef](#)]
55. Walther, S.; Voigt, M.; Thum, T.; Gonsamo, A.; Zhang, Y.; Kohler, P.; Jung, M.; Varlagin, A.; Guanter, L. Satellite Chlorophyll Fluorescence Measurements Reveal Large-Scale Decoupling of Photosynthesis and Greenness Dynamics in Boreal Evergreen Forests. *Glob. Chang. Biol.* **2016**, *22*, 2979–2996. [[CrossRef](#)] [[PubMed](#)]
56. Wang, C.; Guan, K.; Peng, B.; Chen, M.; Jiang, C.; Zeng, Y.; Wu, G.; Wang, S.; Wu, J.; Yang, X. Satellite Footprint Data from OCO-2 and TROPOMI Reveal Significant Spatio-Temporal and Inter-Vegetation Type Variabilities of Solar-Induced Fluorescence Yield in the US Midwest. *Remote Sens. Environ.* **2020**, *241*, 111728.
57. Felton, A.J.; Zavislan-Pullaro, S.; Smith, M.D. Semiarid Ecosystem Sensitivity to Precipitation Extremes: Weak Evidence for Vegetation Constraints. *Ecology* **2019**, *100*, e02572.
58. Huang, J.; Yu, H.; Guan, X.; Wang, G.; Guo, R. Accelerated Dryland Expansion under Climate Change. *Nat. Clim. Chang.* **2016**, *6*, 166.
59. Min, S.-K.; Zhang, X.; Zwiers, F.W.; Hegerl, G.C. Human Contribution to More-Intense Precipitation Extremes. *Nature* **2011**, *470*, 378.
60. Ahlström, A.; Raupach, M.R.; Schurgers, G.; Smith, B.; Arneeth, A.; Jung, M.; Reichstein, M.; Canadell, J.G.; Friedlingstein, P.; Jain, A.K. The Dominant Role of Semi-Arid Ecosystems in the Trend and Variability of the Land CO₂ Sink. *Science* **2015**, *348*, 895–899.
61. Poulter, B.; Frank, D.; Ciais, P.; Myneni, R.B.; Andela, N.; Bi, J.; Broquet, G.; Canadell, J.G.; Chevallier, F.; Liu, Y.Y.; et al. Contribution of Semi-Arid Ecosystems to Interannual Variability of the Global Carbon Cycle. *Nature* **2014**, *509*, 600–603. [[CrossRef](#)] [[PubMed](#)]
62. Morton, D.C.; Nagol, J.; Carabajal, C.C.; Rosette, J.; Palace, M.; Cook, B.D.; Vermote, E.F.; Harding, D.J.; North, P.R. Amazon Forests Maintain Consistent Canopy Structure and Greenness during the Dry Season. *Nature* **2014**, *506*, 221–224. [[CrossRef](#)] [[PubMed](#)]
63. Saleska, S.R.; Wu, J.; Guan, K.; Araujo, A.C.; Huete, A.; Nobre, A.D.; Restrepo-Coupe, N. Dry-Season Greening of Amazon Forests. *Nature* **2016**, *531*, E4–E5. [[CrossRef](#)] [[PubMed](#)]